www.sciencemag.org/content/350/6257/193/suppl/DC1

Supplementary Materials for

Erosion by an Alpine glacier

Frédéric Herman,* Olivier Beyssac, Mattia Brughelli, Stuart N. Lane, Sébastien Leprince, Thierry Adatte, Jiao Y. Y. Lin, Jean-Philippe Avouac, Simon C. Cox

*Corresponding author. E-mail: frederic.herman@unil.ch

Published 9 October 2015, *Science* **350**, 193 (2015)
DOI: 10.1126/science.aab2386

This PDF file includes:

Other Supplementary Materials for this manuscript include the following:
(available at www.sciencemag.org/content/350/6257/193/suppl/DC1)

Materials and Methods

3D glacier velocities

The average 3D velocities were derived from the measurement of the 3D displacement of the glacier surface between each stereo acquisition. Successive stereo acquisitions were used to retrieve the 3D displacement between multi-temporal stereo pairs of Worldview images following the procedure highlighted in section 4.2 and Fig. 10 of Avouac and Leprince (2015) *(33)*. Briefly summarized, each image of each stereo-pair was projected on a flat seed topography, and correlation was applied to associate similar pixels. Correlation between images acquired at similar times was used to measure the topography parallax, and then to recover the topography surface using the satellite position and pointing information. Correlation between multi-temporal images was used to link the topography at each time, and therefore directly deduce the 3D displacement vector.

We used four pairs of Worldview images with a ground sampling distance between 50 and 60 cm (Table S1). Absolute and relative accuracy of image registration was improved using bundle adjustment. We selected between 100 and 300 tie-points between each image pairs, and satellite ancillary data were jointly optimized. Satellite roll, pitch, and yaw angles were corrected with order two polynomials, allowing a maximum ground deviation of 10 m, within specifications of the Worldview satellite accuracy. On average, we detected a mean georeferencing error of 4.3 m with standard deviation of ± 2.5 m, reduced to 16 cm ± 14 cm after bundle adjustment (statistics over 3000 tie-points between all image pairs). Tie-points were selected automatically using sub-pixel correlation, and manual checks were performed to remove tie-points on potentially moving surfaces.

Image matching of all image pairs was performed using a multi-scale approach and semi-global matching regularization *(34-36)*. Similarly, we also used an L_1-norm regularization on the disparity gradient from the correlation maps.

For display of the velocity fields, the 3D velocity vector clouds were gridded on a 1 m grid using nearest neighborhood. For each point, the total

geometric error budget was estimated as the distance between light rays at the point of measurement. On the Franz Josef Glacier surface, the 1-σ velocity errors were estimated to be around ± 7 cm/day.

We show in Fig. S1 the 3D component of the derived velocity field used to compute Fig. 1. Finally, the velocity field was projected along the distance to the sampling station averaged over fixed spatial intervals for comparison with erosion rates (Fig. S2). Note that the reproducibility of the observed velocities between 2013 and 2014 indicates that the integration time for averaging the velocity was sufficiently long.

Water discharge, suspended sediment load and erosion rates

To estimate the erosion rate of the glacier, we continuously monitored water discharge (i.e., every 5 minute time interval) and suspended load of the glacial stream using a calibrated automated stream gauge installed 1.2 km away from the glacier terminus (from November 24, 2013 to April 9, 2014). The results are shown in Fig. S3, along with precipitation rates measured at the Franz Josef NIWA weather station. From such measurements, one can compute erosion rates using the following relationship

$$Q_s(t) = \int \rho_s \dot{e}\, dA \; - \; \rho_b \frac{dV}{dt} \qquad (1)$$

where Q_s is the sediment load (g s^{-1}), ρ_s is the density of the subglacial bedrock (2700 kg m^3 *(37)*), $\dot{e}$ is the erosion rate (m s^{-1}), A is the area of the glacier (m^2), ρ_b is the density of subglacially stored sediments (kg m^{-3}) and $\frac{dV}{dt}$ is the volumetric change of sediments within the glacier.

A close analysis of water discharge and suspended sediment load during rain events reveal classical hysteresis loops (Fig. S4). Such an observation testifies for a supply-limited system *(20)*, at least for the regions where pipes or channels run along the bed. This implies that the volumetric change of sediments is negligible and, therefore, our measured suspended sediment load can be used as a proxy for glacial erosion. This is further supported by observed erosion rates of about 10 mm/yr over the 5-month period that closely matches Myr erosion rates in the area *(e.g. 30)*. Note that Riihimaki et al. (2005) *(20)* also assumed that volumetric change is close to zero for the Bench Glacier, Alaska. Given that the

precipitation rates, water discharge and ice velocities are all an order of magnitude larger for the Franz Josef Glacier, it is not surprising to infer negligible volumetric changes.

To quantify spatial variations in erosion rates, we determine the provenance of the suspended sediments collected at the gauge using Raman Spectroscopy of Carbonaceous Material *(27)* (RSCM; see next section). Using Eqn. (1), we can in turn derive erosion rate as a function of horizontal distance to the sampling station, x, as follows

$$\dot{e}(x,t) \approx \frac{f(x,t)}{\Delta x} \frac{Q_s(t)/\rho_s}{C_t(x)\, w(x)} \quad (2)$$

where $f(x,t)$ is the relative frequency of the mineral provenance, Δx (m) is the bin size used to compute the frequency distribution, C_t is the bedrock concentration of the tracer, i.e., total organic content *(26)*, and *w(x)* (m) is the glacier width with horizontal distance. To calculate $f(x,t)$, we use the extensive bedrock RCSM temperature data (Table S2), which we linearly interpolate within the catchment (Fig. S5A) and then project the interpolation along the distance to the sampling station. Temperatures are then converted to distance to the sampling station using the following equation

$$T = T_0 + T_1 \left[1 - \left(\text{atan}\left(\frac{x-x_0}{\lambda}\right)\frac{2}{\pi}\right)/2\right] \quad (3)$$

where T_0, T_1, x_0, λ and are arbitrary parameters optimized using the non-linear least squares method (using the function *lsqnonlin* in the Matlab software). The results are shown in Fig. S5B, where T_0= 333, T_1= 243.5, x_0= 5005.27, λ=5005.27.

Finally, it is worth noting that the uncertainty on the reconstructed erosion profile (Fig. S2A) is substantially larger than the geometric corrections used to reconstruct the one-dimensional profile.

Raman Spectroscopy of Carbonaceous Material (RSCM)

Details on the application of Raman spectroscopy to the study of rock-derived fossil organic carbon including thermometry are given in Beyssac et al. (2002) *(27)* and Beyssac and Lazzeri (2012) *(38)*. Here the approach consists of comparing the structure of rock-derived fossil organic carbon in the suspended load of the glacial stream to that of fossil organic carbon in the bedrock. For the

sake of clarity, we convert the Raman parameters describing the degree of graphitization into peak metamorphic temperatures using the equations provided by Beyssac et al. (2002) *(27)* and Lahfid et al. (2010) *(39)*. RSCM has already been applied to the study of rock-derived fossil organic carbon in suspended loads of rivers in the Himalayan *(40)* and Amazonian systems *(41)* to establish global carbon budget of erosion, but not for provenance analysis.

We collected a total of 167 water samples in the glacial stream during the 5-month field campaign. We used a depth-integrated sampler fitted with an isokinetik nozzle, that allows us to account for the vertical grain size distribution within the glacial stream. The sample (473.17 mL) was then fitted with a 47 mm diameter and 0.22 μm hydrophilic filter and pressurized at 2.5 bar using a manual pump. RSCM analyses were performed on 14 samples, which were carefully chosen to cover a broad range of weather conditions (Movie S1). Raman analysis of the sediments was measured directly on the sample raw powder without any chemical or mechanical extraction thus preserving the pristine structure of fossil organic carbon.

Raman spectra were obtained with point measurements by using a Renishaw InVia Reflex instrument. This system is equipped with a Leica DMLM microscope, a grating with 1800 grooves per millimeter, and a charge-coupled device detector. Spectra were excited using the 514.5 nm emission line of an argon laser (<1 mW measured at the sample surface) with a circular polarization thanks to a quarter wavelength plate set in the optical path before the microscope. We used a long-working distance Leica objective x50 (numerical aperture of 0.75) yielding a lateral resolution of nearly 1 μm. The spectral resolution of the system is estimated at around 1.5 cm^{-1} in the configuration used. Wavenumber calibration was done using a silicon standard and Ne lamp emission. On each sample, we collected 200-250 Raman Spectra to have statistically significant data. The observed Raman spectra were then fitted following the procedure described in Beyssac and Lazerri (2012) *(38)*, Lahfid et al. (2010) *(39)* and Sparkes et al. (2013) *(42)*.

Constraining the erosion law

Our goal is to estimate the parameters K_g and l from the erosion law

$$\dot{e} = K_g \, |u_s|^l \tag{4}$$

where both u_s and $\dot{e}$ are a function of distance to the sampling station. We first compute the mean and standard deviation of the observed erosion rates, assuming it follows a lognormal distribution, and ice velocities. We assume a log normal distribution because erosion rates have a mean value that is low, a large variance, and cannot be negative, which is typical of lognormal distribution *(43).*

We used two independent methods to constrain K_g and l. First, we use a Bayesian approach to construct probability density functions (PDFs) of K_g and l. The quality of fit to the data is estimated through the following likelihood function:

$$\mathcal{L} = \exp\left(-\frac{1}{2}\sum\left|\frac{\varepsilon_m - \varepsilon_o}{\sigma}\right|^2\right) \tag{5}$$

where ε is natural logarithm of $\dot{e}$, such that

$$\varepsilon_m = \ln\left(K_g\right) + l \ln\left(|u_s|\right) \tag{6}$$

and σ is the standard deviation on the observed erosion rates, on a logarithmic scale, and m and o stand for modeled and observed erosion. Then, the likelihood solution is resampled to estimate the PDFs using a standard rejection algorithm. From these PDFs one can estimate the 90 and 60% confidence interval. The results are shown in Fig. 3.

Second, we use the non-linear least squares method using the Matlab software, which led to K_g=2.5 10^{-7} $(\mathrm{m/yr})^{1-l}$ and l=2.02.

Glacial flow model

To illustrate the response of glacial erosion to changes in precipitation, we present the results of a simple thought numerical experiment in which we progressively increase the accumulation rate. Our goal is not to model the Franz Josef glacier but to illustrate the impact of changing precipitation on erosion rates.

To model glacial flow, we first compute the ice thickness, h, by solving the equation of mass conservation:

$$\frac{\partial h}{\partial t} = M - \nabla \cdot \mathbf{q} \tag{7}$$

where **q** is the vertically averaged ice flux (**q**=h**u**, where **u** is the vertically integrated horizontal ice velocity) and M the surface mass balance. The ice velocity, **u**, is the sum of the deformation velocity, $\mathbf{u_d}$, and the sliding velocity, $\mathbf{u_s}$. The shallow ice approximation *(44,45)* is used to compute Eqn. 7,

$$\frac{\partial h}{\partial t} = M - \nabla \cdot [(f_d\,(\rho g)^n h^{n+2} + f_s\,(\rho g)^n h^n)]|\nabla(h+z)|^{n-1}\nabla(h+z) \quad (8)$$

where f_d is the ice flow-law parameter (1.9 10^{-24} Pa^{-3} s^{-1}), f_s is the sliding law parameter (5.7 10^{-20} Pa^{-3} m^2 s^{-1}), ρ is the density of the ice (910 kg m^{-3}), g is the gravitational acceleration (9.81 m s^{-2}), n Glen's Flow parameter (3), and z the bedrock topography. Eqn. 8 is solved using the finite difference method. The model is run until steady state is reached and using a spatial resolution of 200 m. The sliding velocity, $\mathbf{u_s}$, is then calculated as follows

$$\mathbf{u_s} = f_s\,(\rho g)^n h^{n-1}|\nabla(h+z)|^{n-1}\nabla(h+z). \quad (9)$$

The mass balance M, is simply prescribed as a function of elevation with a maximum accumulation rate, as typically observed in mountain glaciers *(e.g. 31)* and in particular the Franz Josef glacier *(24)*. Finally, erosion rate is calculated using Eqn. (4) and prescribing a bedrock topography that decreases linearly from 3000 m a.s.l down to sea level over 10 km.

We show in Fig. S6 two simulations in which we impose maximum ice accumulation rate of 1 m/yr and 7 m/yr, respectively. These simple thought experiments show that changes in accumulation rate lead to larger variations in erosion rates when the erosion law is non-linear.

Negligible contribution from hillslopes during the investigation period

The possible contribution of surrounding hillslopes was further investigated by X-ray diffraction and Total Organic Carbon (TOC) analysis on 16 samples. The bulk-rock mineralogy of the samples was determined by X-ray diffraction *(46)*. The results show that clay minerals are far less significant than metamorphic phyllosilicates. Trace level contents (i.e. < 2 %wt) of biotite-vermiculite mixed layers (i.e. hydrobiotite) and vermiculite resulting from weathering of biotite are systematically observed, but reflect a negligible contribution *(46,47)* from the hillslopes compared to glacial erosion. Garnet, a constituent mineral of the rocks metamorphosed >525°C that form hillslopes at the snout of the glacier and

immediately adjacent to the sampling site, could not be found in XRD traces of the suspended sediment.

TOC analysis was carried out with a Rockeval 6. In this technique, bulk dried samples are heated in an inert atmosphere and, upon pyrolysis, the main emission products (hydrocarbons, CO_2, CO) are quantified by flame-ionization and infrared detection *(48,49)*. These measurements are used to calculate several parameters: TOC content (analytical error: +-0.1%), Pyrolized Carbon, Residual Carbon and Hydrogen Index (mg HC/g TOC). Pyrolized Carbon and Hydrogen Index reflect the amount of soil organic matter *(50)*, whereas Residual Carbon values mainly reflect residual fossil graphitic carbon from the erosion of metamorphic rocks. Here we observe that Residual Carbon components (mean value: 0.14) are substantially larger than the Pyrolized Carbon components (mean value: 0.03), indicating that TOC is mainly derived from bedrock. The low soil-derived TOC inputs therefore confirmed the mineralogical composition of the suspended sediments, in which soil-derived clay minerals (vermiculite) represent only a negligible contribution. Importantly, the Hydrogen Index is inversely proportional to the suspended sediment load (Fig. S7), which implies that the contribution of modern carbon from the side-slopes is decreasing during rain events. This suggests that the contribution from soils found on hillslopes is small compared to glacial erosion over the period of investigation.

If hillslope erosion were dominating through another process, one would expect it to be maximized where the slopes are highest (Fig. S8). We would then predominantly see material coming from in between the glacier front and the sampling station (i.e., where rocks are garnet zone schist and RSCM temperatures are >525°C). Instead, the suspended sediment load contains only a very small fraction of material sourced from such high temperature rocks (Movie S2). Alternatively, sediment supply from hillslopes may be stochastic, as landsliding is known to be a dominant hillslope erosion process in the Southern Alps *(26,51,52)*. There were no large landslides or rock avalanches in the valley during the 5-month field campaign. Visible erosion scars and debris-flow channels are present on slopes either side of the glacier (between Croz Glacier-Cape Defiance on the true left and Hende Ridge-Roberts point on the true right). Fluvial processes during periods of intense rain and sporadic rock falls may

carry material from these slopes onto and underneath the glacier. But the rocks here are strongly-foliated biotite and garnet zone schist *(25),* in which RSCM temperatures are higher than 500°C. If there were large quantities of rocks derived from these slopes, it would enhance the content of carbonaceous material that experienced temperatures higher than 500°C in the suspended sediment. Instead, the majority of this material was sourced from rock metamorphosed at between 400 and 500°C (Movie S2), being greenschist or biotite zone schists, that are found where the glacier is most rapidly sliding and the slopes adjacent to the glacier are of comparatively small extent. Furthermore, the glacier is clean of debris in that section.

Steady drainage system at Franz Josef

To further contrast the behavior of the Franz Josef glacier with an alpine glacier that exhibits changes in the drainage system, we compare the Franz Josef discharge hydrograph with that of the Swiss Haut Glacier d'Arolla, which is known to see its drainage system to evolve during the melt season *(53)*. As the subglacial drainage system evolves from a cavity, poorly connected system to a more efficient channelized system, the hydrograph becomes substantially different for the Haut Glacier d'Arolla (Fig. S9). In contrast, we observe no change for the Franz Josef Glacier. This observation further implies that there is no systematic development of the subglacial drainage system at Franz Josef during the investigation period.

Finally, Anderson et al. (2014) *(29)* recently reached similar conclusions by showing that the Franz Josef glacier remains highly responsive to precipitation.

Surface velocities dominated by sliding

To assess the assumption that surface velocities are dominated by sliding, we ran four tests in which we assume that the sliding velocity is 25, 50, 75 and 100 % of the surface velocity (Fig. S10). It shows that this assumption has little impact on the estimate of the erosion exponent l. The fit to data is mostly accommodated by a change in K_g.

SOM Figures

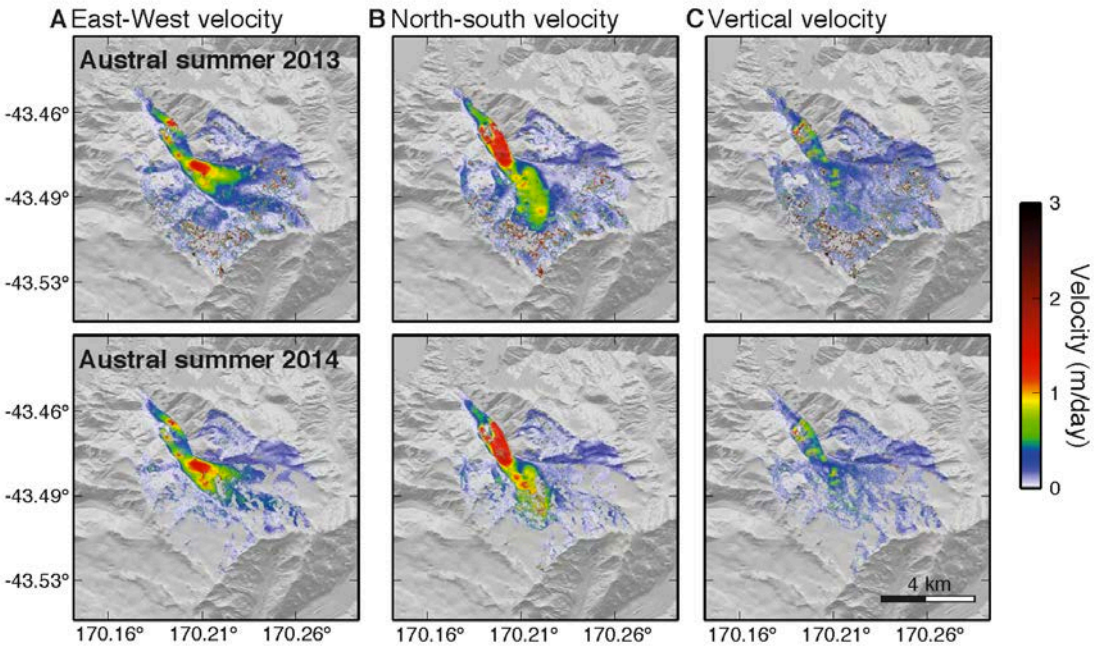

Figure S1. 3D components of the velocity field shown in Fig. 1. (A) East-west absolute velocity, **(B)** north-south absolute velocity and **(C)** vertical absolute velocity. The upper panels depict the surface velocity measured in summer 2013, and the lower panels those in summer 2014.

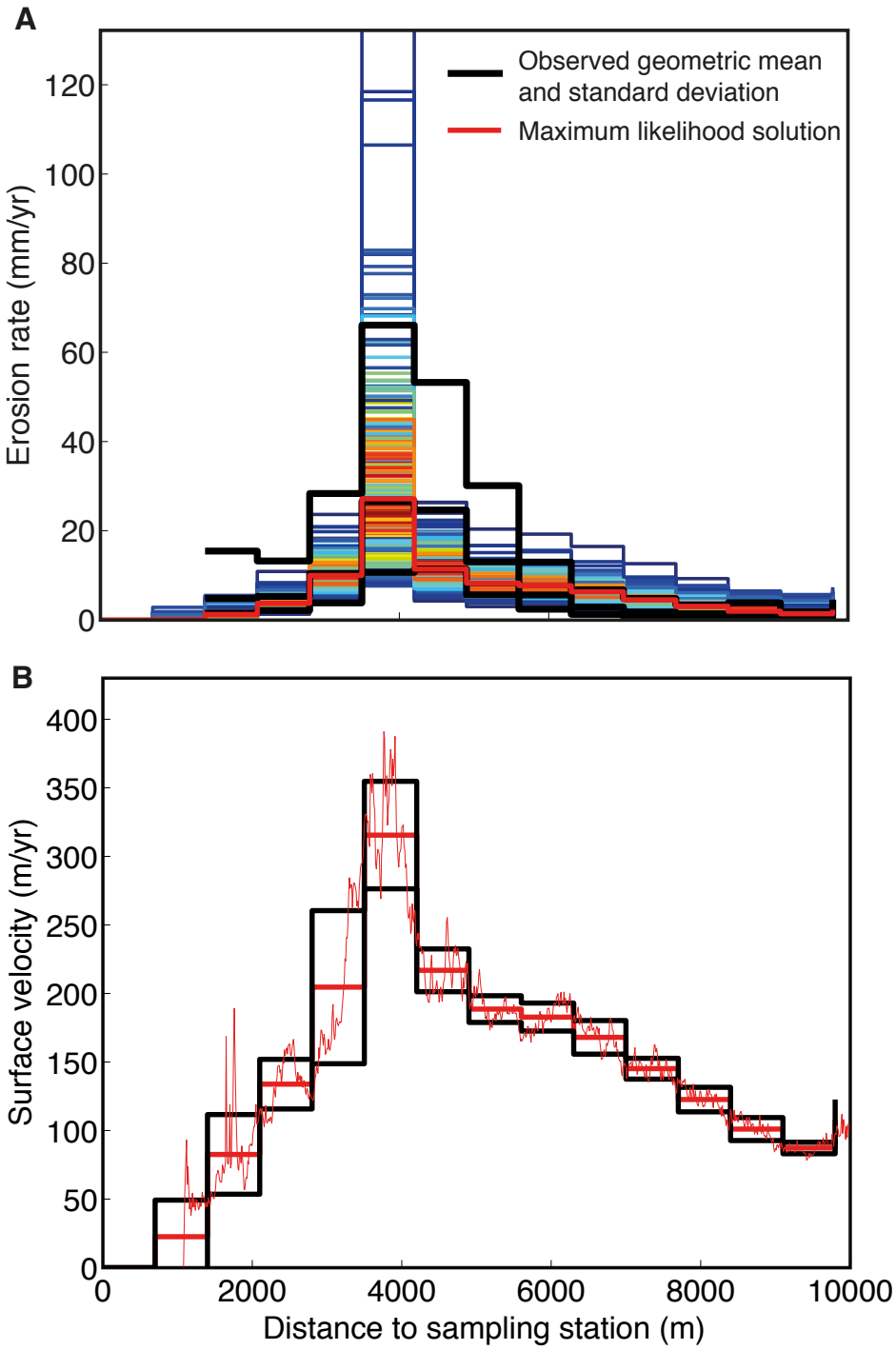

Figure S2. Fit to observations and 1d- velocity field. (A) Comparison between modeled and observed erosion rates. The black lines represent the geometric mean ± 1-σ standard deviation, assuming erosion rate follow a lognormal distribution. The blue to red lines represent the modeled erosion rates using K_g and l shown in (Fig. 3B). **(B)** 2014 velocities projected along the distance from the sampling station.

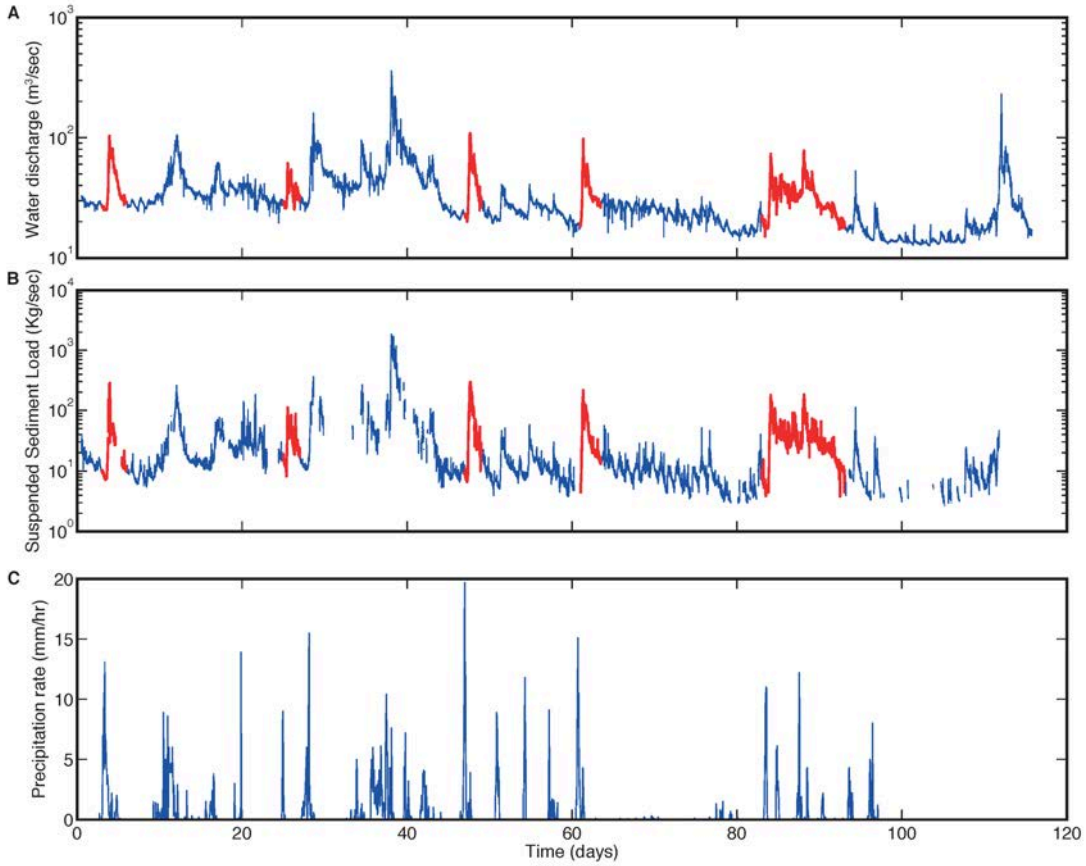

Figure S3. Measured hydrological parameters. (A) Water discharge, **(B)** suspended sediment load and **(C)** precipitation rates as a function of time (i.e. number of days since November 24, 2013). Red lines in **(A)** and **(B)** correspond data presented in Fig. S4.

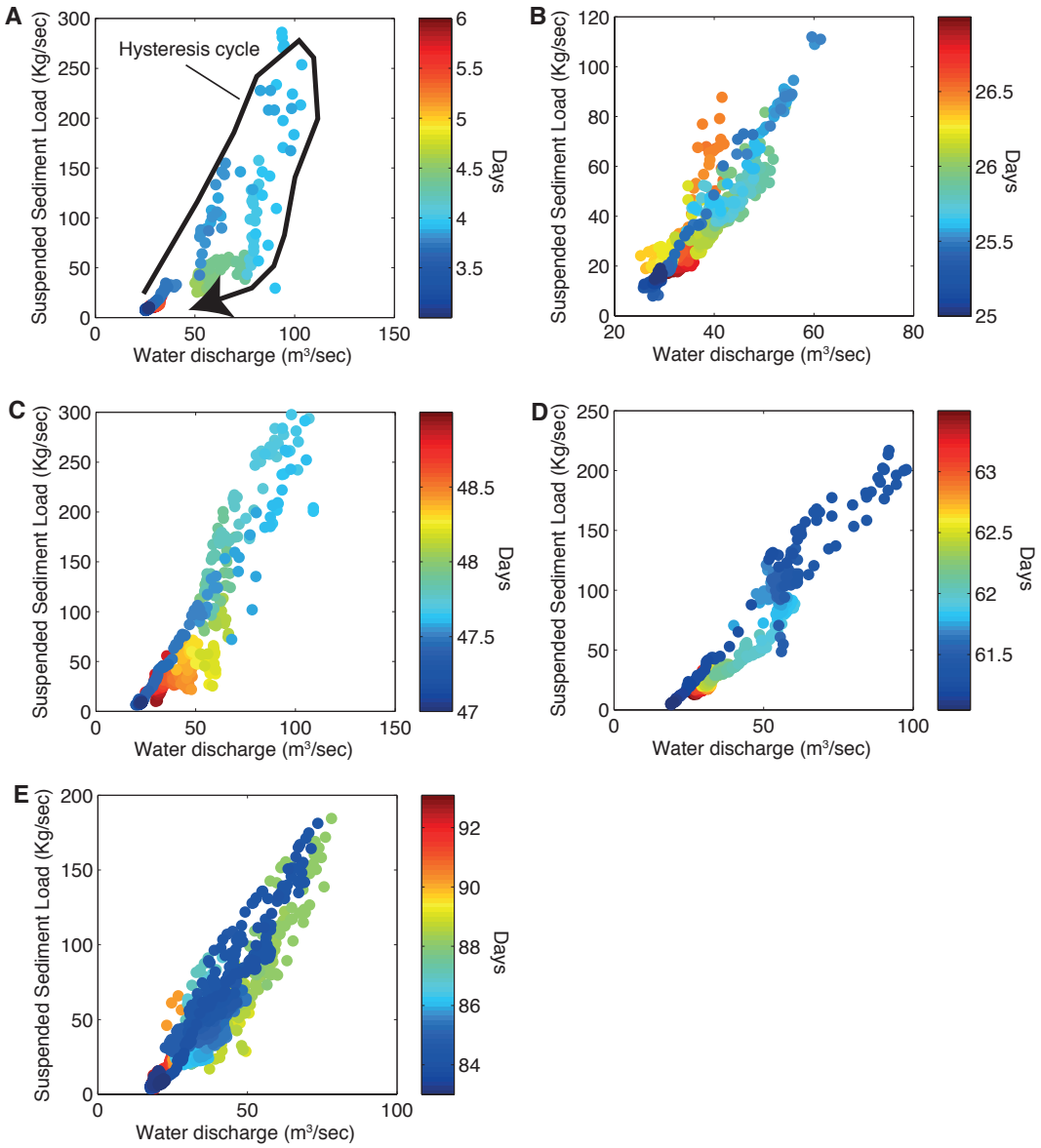

Figure S4. Hysteresis diagrams. (A) to **(E)** correspond to the section highlighted in red in Fig. S3. It shows that sediment concentration is higher at the beginning of the rain event and then decreases throughout the period of anomalous discharge. The color bar is associated with the days shown on the x-axis of Fig. S3. This observation indicates that the system is supply-limited *(20)*.

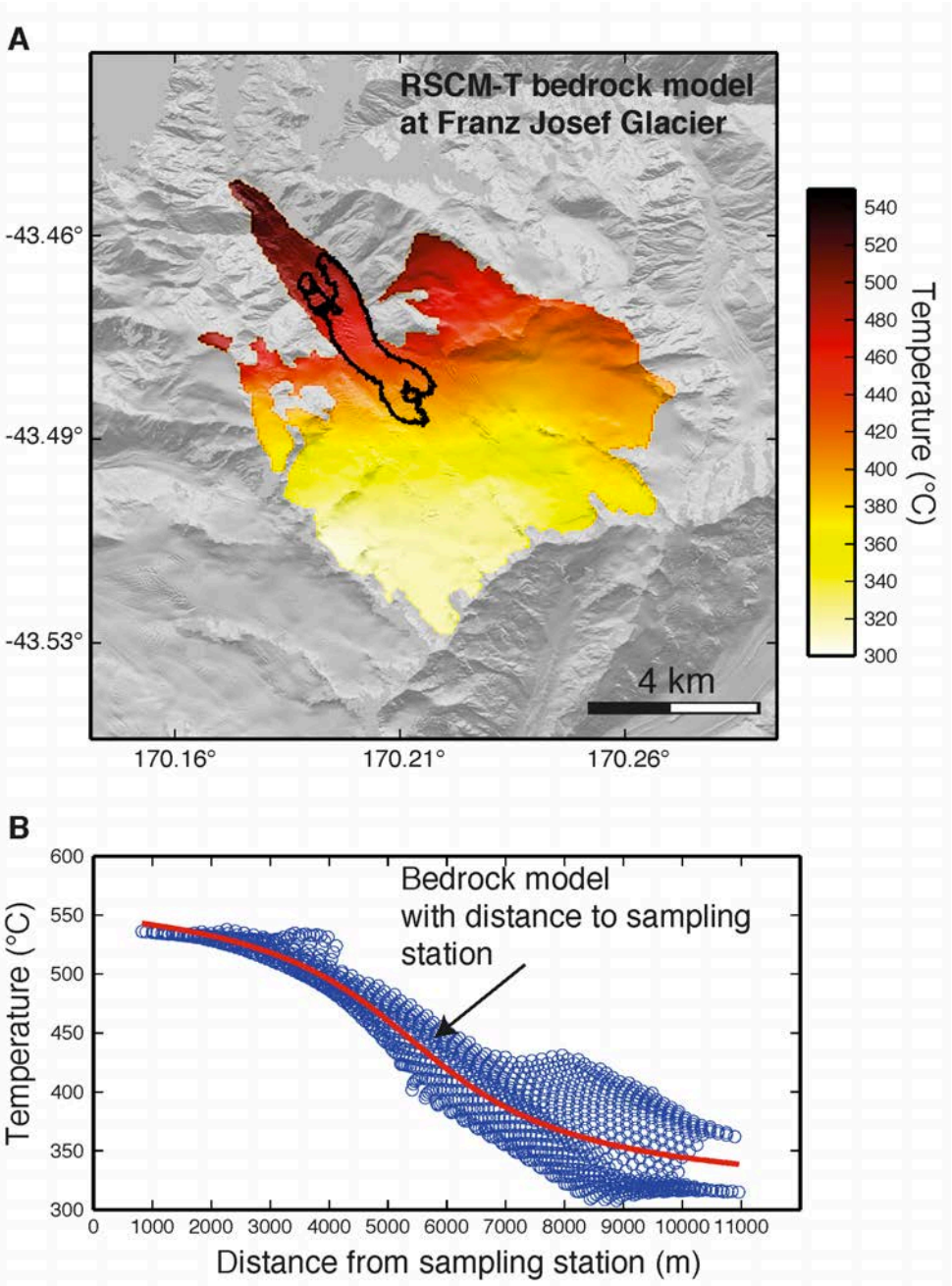

Figure S5. RSCM bedrock model. (A) Interpolated bedrock temperature model underneath the glacier using data from Table S2 and shown in Fig. 2. The black contour line highlights the region where the velocity is higher than 1.25 m/day in Fig. 1. **(B)** 1-dimensional temperature model used for the provenance analysis.

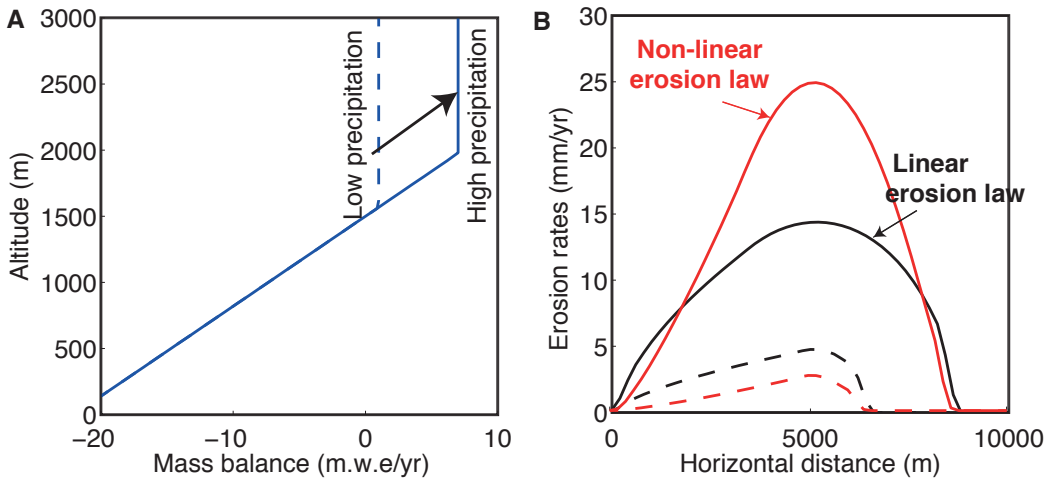

Figure S6. Glacial erosion numerical experiments. To model glacial erosion, we compute the ice thickness by solving the mass conservation equation. The ice thickness results from the difference between the divergence of the ice flow and altitudinal mass balance. **(A)** Imposed altitudinal mass balance. Ice accumulation rate is increased from 1 m/yr to 7 m/yr. **(B)** Black lines depict predicted erosion rates with l=1 and K_g=4.8 10^{-5} and red lines predicted erosion rates with l=2.02 and K_g=2.7 10^{-7} (m^{1-l}/yr^{1-l}). K_g and l are derived correspond to results reported in Fig. 3. Dotted lines are for low precipitation and solid lines for high precipitation.

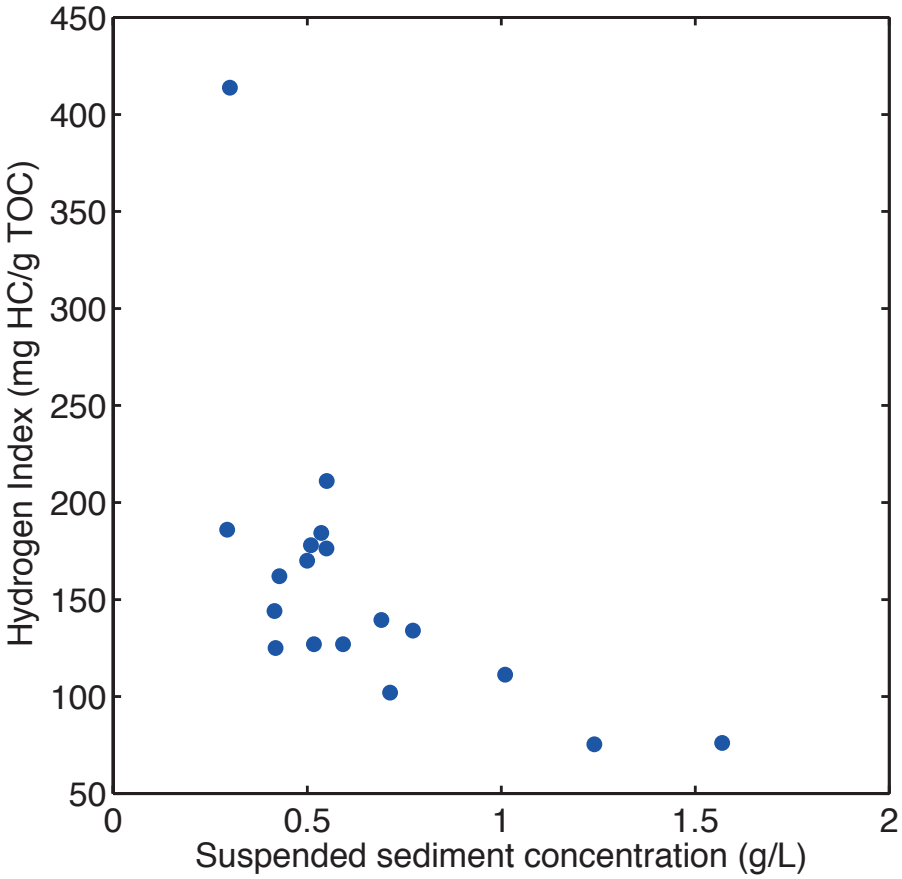

Figure S7. RockEval and TOC analyses. Suspended sediment concentration versus Hydrogen Index. The reduction of Hydrogen Index with increasing sediment concentration indicates that the contribution from hillslopes is negligible compared to glacial erosion.

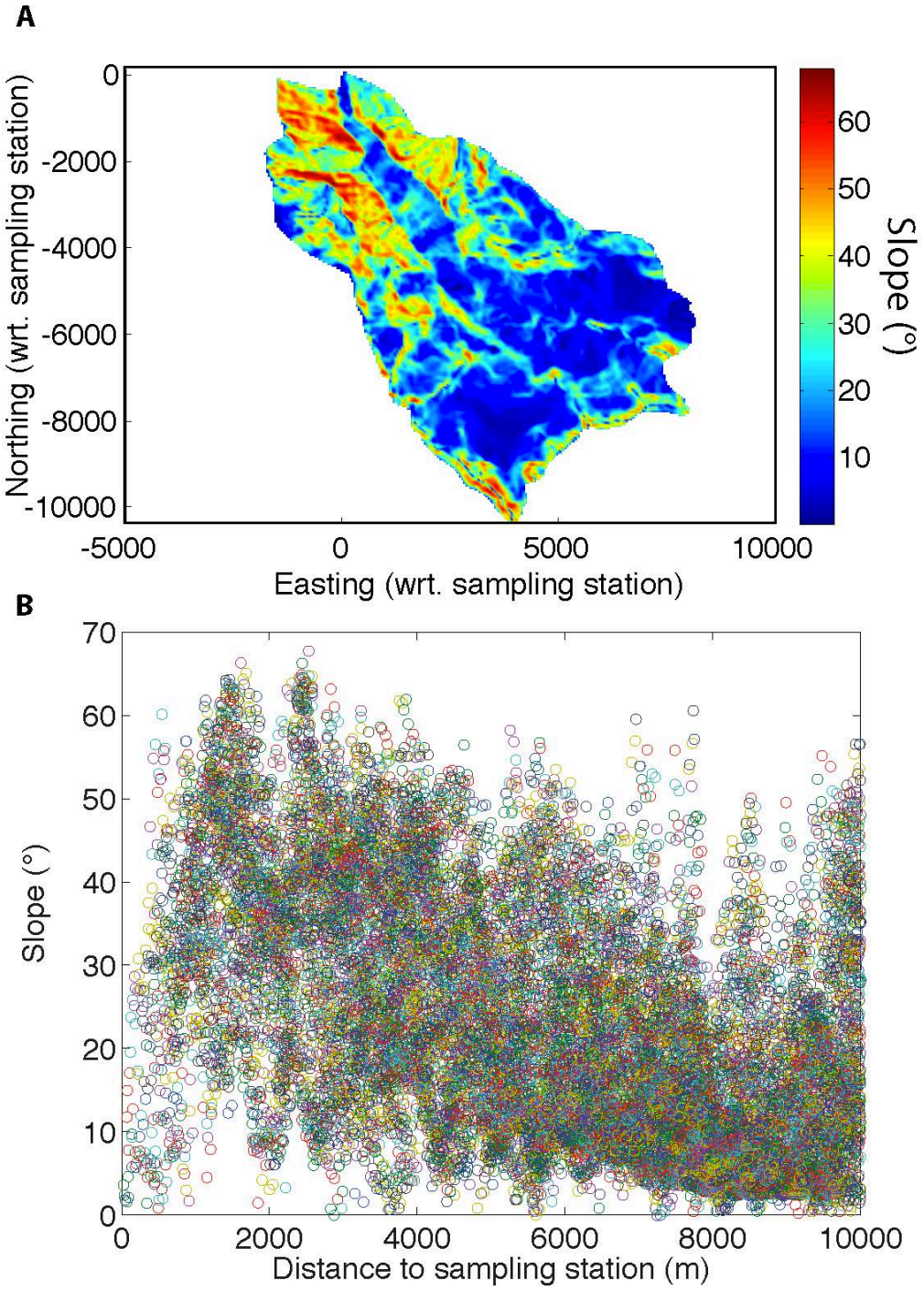

Figure S8. Slopes. (A) Steepest slope over the entire Waiho catchment plotted in map view (from the sampling station). **(B)** Same as (A) but with distance to the sampling stations. It shows that the steepest hillslopes are found toward the sampling station.

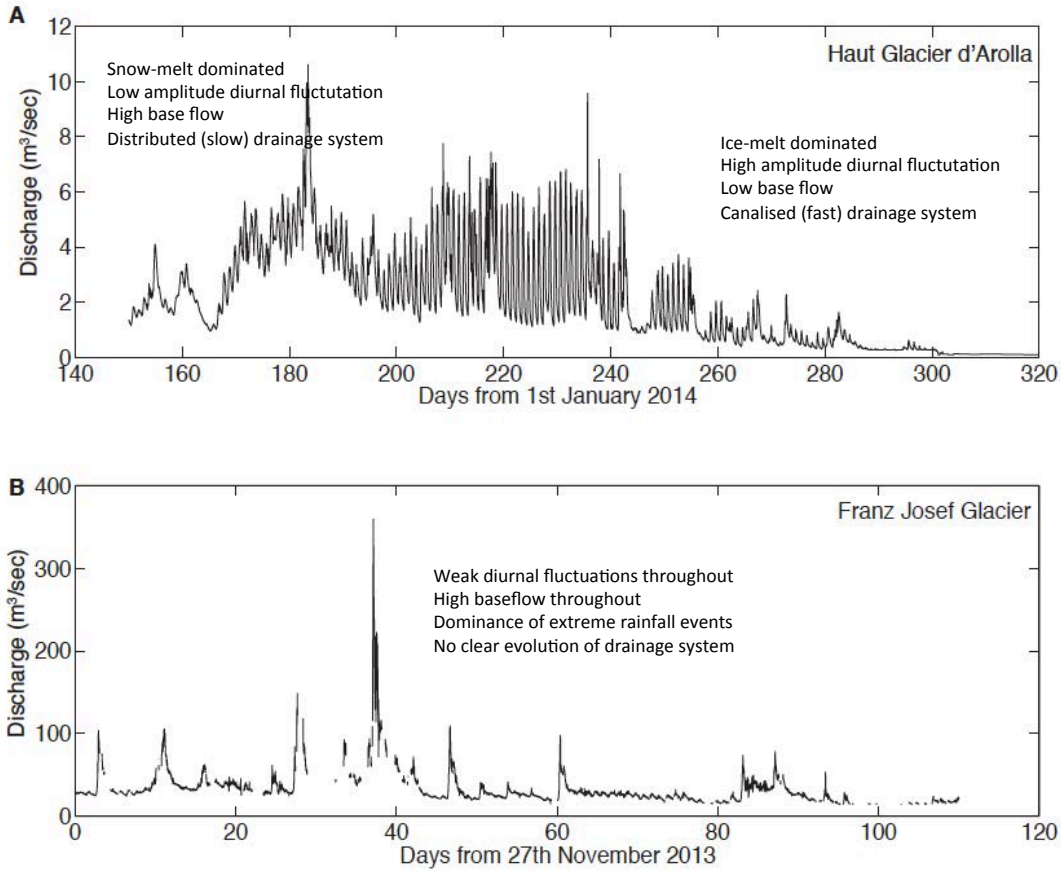

Figure S9. Hydrographs for the Haut Glacier d'Arolla and the Franz Josef Glacier. Comparison of water discharge measurements from winter to summer **(A)** at the Haut Glacier d'Arolla, Switzerland (the data were provided by Hydroexploitation on behalf of Grande SA) and **(B)** at the Franz Josef Glacier. The change in water discharge observed at the Haut Glacier d'Arolla reflects a transition from cavity-driven flow to channelized flow. For the Franz Josef glacier, no change is observed throughout the melt season.

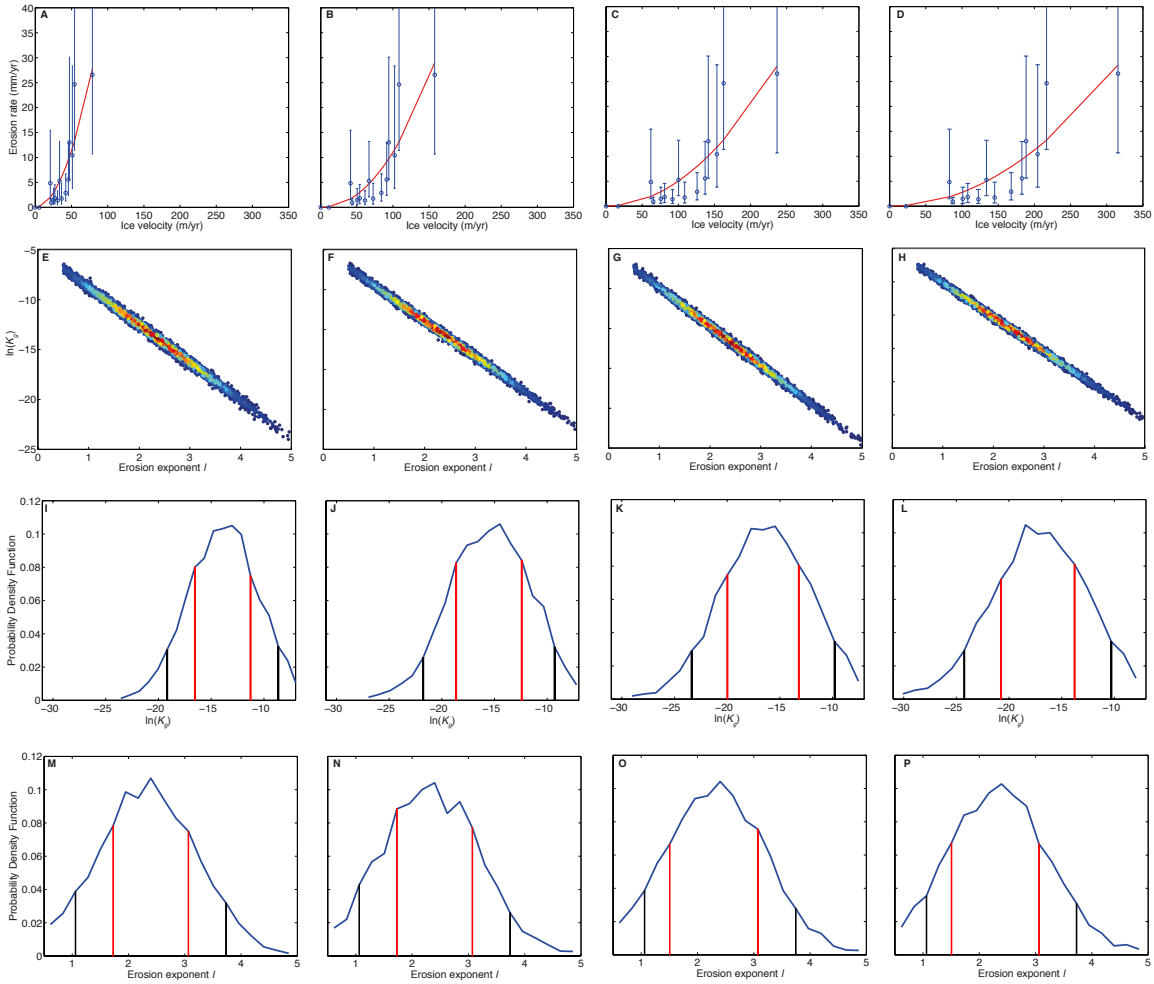

Figure S10. Inferred K_g and l for different sliding velocities. See caption of Fig. 3 for details on the plots. **(A),(E), (I)** and **(M)** are inferred parameters assuming that the sliding velocity is 25% of the surface velocity, **(B), (F), (J)** and **(N)** is 50% of surface velocity, **(C), (G), (K)** and **(O)** is 75% of the surface velocity and **(D), (H), (L)** and **(P)** for 100% of the surface velocity. Red lines in **(A)** were fitted with K_g and l equal to 5.39 10^{-7} (m^{1-l}/yr^{1-l}) and 1.95, 6.55 10^{-7} (m^{1-l}/yr^{1-l}) and 2.11 in **(B)**, 5.18 10^{-7} (m^{1-l}/yr^{1-l}) and 1.99 in **(C)**, 2.57 10^{-7} (m^{1-l}/yr^{1-l}) and 2.02 in **(D).**

SOM Tables

Table S1. Worldview stereo-pairs for each date (month.day.year).

Table S2. Bedrock RSCM temperature.

SOM Movies

Movie S1. Upper panel shows erosion rates with distance from the sampling station for each day shown with the magenta dot in the bottom panel. The middle panel shows the erosion rate integrated over the glacier. The bottom panel is the precipitation rate. The x-axis for middle and bottom panels corresponds to the number of days since November 24, 2013.

Movie S2. Relative frequency of RSCM temperature used to infer the erosion patterns shown in Movie S1. It shows that most of the measured RSCM temperature are between 400 and 500°C.

.

.

.

.

REFERENCES AND NOTES

1. P. Molnar, P. England, Late Cenozoic uplift of mountain ranges and global climate change: Chicken or egg? *Nature* **346**, 29–34 (1990). doi:10.1038/346029a0

2. J. H. Tomkin, G. H. Roe, Climate and tectonic controls on glaciated critical-taper orogens. *Earth Planet. Sci. Lett.* **262**, 385–397 (2007). doi:10.1016/j.epsl.2007.07.040

3. J. Braun, D. Zwartz, J. H. Tomkin, A new surface-processes model combining glacial and fluvial erosion. *Ann. Glaciol.* **28**, 282–290 (1999). doi:10.3189/172756499781821797

4. F. Herman, D. Seward, P. G. Valla, A. Carter, B. Kohn, S. D. Willett, T. A. Ehlers, Worldwide acceleration of mountain erosion under a cooling climate. *Nature* **504**, 423–426 (2013). Medline doi:10.1038/nature12877

5. B. Hallet, A theoretical model of glacial abrasion. *J. Glaciol.* **17**, 209–222 (1979).

6. B. Hallet, Glacial quarrying: A simple theoretical model. *Ann. Glaciol.* **22**, 1–8 (1996).

7. N. R. Iverson, A theory of glacial quarrying for landscape evolution models. *Geology* **40**, 679–682 (2012). doi:10.1130/G33079.1

8. J. Harbor, B. Hallet, C. F. Raymond, A numerical model of landform development by glacial erosion. *Nature* **333**, 347–349 (1988). doi:10.1038/333347a0

9. K. R. MacGregor, R. S. Anderson, S. P. Anderson, E. D. Waddington, Numerical simulations of glacial-valley longitudinal profile evolution. *Geology* **28**, 1031–1034 (2000). doi:10.1130/0091-7613(2000)28<1031:NSOGLP>2.0.CO;2

10. D. L. Egholm, S. B. Nielsen, V. K. Pedersen, J. E. Lesemann, Glacial effects limiting mountain height. *Nature* **460**, 884–887 (2009). Medline doi:10.1038/nature08263

11. K. R. MacGregor, R. S. Anderson, E. D. Waddington, Numerical modeling of glacial erosion and headwall processes in alpine valleys. *Geomorphology* **103**, 189–204 (2009). doi:10.1016/j.geomorph.2008.04.022

12. M. A. Kessler, R. S. Anderson, J. P. Briner, Fjord insertion into continental margins driven by topographic steering of ice. *Nat. Geosci.* **1**, 365–369 (2008). doi:10.1038/ngeo201

13. F. Herman, F. Beaud, J.-D. Champagnac, J.-M. Lemieux, P. Sternai, Glacial hydrology and erosion patterns: A mechanism for carving glacial valleys. *Earth Planet. Sci. Lett.* **310**, 498–508 (2011). doi:10.1016/j.epsl.2011.08.022

14. T. T. Creyts, G. K. C. Clarke, M. Church, Evolution of subglacial overdeepenings in response to sediment redistribution and glaciohydraulic supercooling. *J. Geophys. Res.* **118**, 423–446 (2013). doi:10.1002/jgrf.20033

15. F. Beaud, G. E. Flowers, S. Pimentel, Seasonal-scale abrasion and quarrying patterns from a two-dimensional ice-flow model coupled to distributed and channelized subglacial drainage. *Geomorphology* **219**, 176–191 (2014). doi:10.1016/j.geomorph.2014.04.036

16. R. B. Alley, D. E. Lawson, G. J. Larson, E. B. Evenson, G. S. Baker, Stabilizing feedbacks in glacier-bed erosion. *Nature* **424**, 758–760 (2003). Medline doi:10.1038/nature01839

17. B. Hallet, L. Hunter, J. Bogen, Rates of erosion and sediment evacuation by glaciers: A review of field data and their implications. *Global Planet. Change* **12**, 213–235 (1996). doi:10.1016/0921-8181(95)00021-6

18. M. N. Koppes, D. R. Montgomery, The relative efficacy of fluvial and glacial erosion over modern to orogenic timescales. *Nat. Geosci.* **2**, 644–647 (2009). doi:10.1038/ngeo616

19. N. F. Humphrey, C. F. Raymond, Hydrology, erosion and sediment production in a surging glacier: Variegated Glacier, Alaska, 1982-83. *J. Glaciol.* **40**, 539–552 (1994).

20. C. A. Riihimaki, K. R. MacGregor, R. S. Anderson, S. P. Anderson, M. G. Loso, Sediment evacuation and glacial erosion rates at a small alpine glacier. *J. Geophys. Res.* **110**, F03003 (2005). doi:10.1029/2004JF000189

21. D. A. Swift, P. W. Nienow, T. B. Hoey, Basal sediment evacuation by subglacial meltwater: Suspended sediment transport from Haut Glacier d'Arolla, Switzerland. *Earth Surf. Process. Landf.* **30**, 867–883 (2005). doi:10.1002/esp.1197

22. J. Oerlemans, Climate sensitivity of Franz Josef Glacier, New Zealand, as revealed by numerical modeling. *Arct. Alp. Res.* **29**, 233–239 (1997). doi:10.2307/1552052

23. Materials and methods are available as supplementary materials on *Science* Online.

24. B. Anderson, W. Lawson, I. Owens, B. Goodsell, Past and future mass balance of 'Ka Roimata o Hine Hukatere' Franz Josef Glacier, New Zealand. *J. Glaciol.* **52**, 597–607 (2006). doi:10.3189/172756506781828449

25. S.C. Cox, D. J. A. Barrell, *Geology of the Aoraki Area* (1:250,000 geological map 15, Institute of Geological and Nuclear Sciences, GNS Science, Lower Hutt, New Zealand, 2007), 71 pp. + 1 folded map.

26. R. G. Hilton, A. Galy, N. Hovius, Riverine particulate organic carbon from an active mountain belt: Importance of landslides. *Global Biogeochem. Cycles* **22**, GB1017 (2008). doi:10.1029/2006GB002905

27. O. Beyssac, B. Goffé, C. Chopin, J. N. Rouzaud, Raman spectra of carbonaceous material in metasediments: A new geothermometer. *J. Metamorph. Geol.* **20**, 859–871 (2002). doi:10.1046/j.1525-1314.2002.00408.x

28. R. L. Hooke, Positive feedbacks associated with erosion of glacial cirques and overdeepenings. *Geol. Soc. Am. Bull.* **103**, 1104–1108 (1991). doi:10.1130/0016-7606(1991)103<1104:PFAWEO>2.3.CO;2

29. B. Anderson, I. Willis, B. Goodsell, A. Banwell, I. Owens, A. Mackintosh, W. Lawson, Annual to daily ice velocity and water pressure variations on Ka Roimata o Hine Hukatere (Franz Josef Glacier), New Zealand. *Arct. Antarct. Alp. Res.* **46**, 919–932 (2014). doi:10.1657/1938-4246-46.4.919

30. T. A. Little, S. Cox, J. K. Vry, G. Batt, Variations in exhumation level and uplift rate along the oblique-slip Alpine fault, central Southern Alps, New Zealand. *Geol. Soc. Am. Bull.* **117**, 707 (2005). doi:10.1130/B25500.1

31. K. M. Cuffey, W. S. B. Paterson, *The Physics of Glaciers* (Butterworth-Heinemann/Elsevier, Oxford, ed. 4, 2010).

32. G. H. Denton, R. F. Anderson, J. R. Toggweiler, R. L. Edwards, J. M. Schaefer, A. E. Putnam, The last glacial termination. *Science* **328**, 1652–1656 (2010). Medline

33. J.-P. Avouac, S. Leprince, in *Treatise on Geophysics*, G. Schubert, Ed. (Elsevier, Oxford, ed. 2, (2015), vol. 3, pp. 387–424.

34. H. Hirschmuller, Accurate and efficient stereo processing by semi-global matching and mutual information. *IEEE Comp. Soc. Conf. Comp. Vision Pattern Recognition*, **2**, 807–814 (2005).

35. H. Hirschmüller, D. Scharstein, Evaluation of stereo matching costs on images with radiometric differences. *IEEE Trans. Pattern Anal. Mach. Intell.* **31**, 1582–1599 (2009). Medline doi:10.1109/TPAMI.2008.221

36. M. Pierrot-Deseilligny, N. Paparoditis, A multiresolution and optimization-based image matching approach: An application to surface reconstruction from SPOT5-HRS stereo imagery. *Archives of Photogrammetry, Remote Sensing and Spatial Information Sciences* 36.1/W41 (2006).

37. T. Hatherton, A. E. Leopard, The densities of New Zealand rocks. *N.Z. J. Geol. Geophys.* **7**, 605–625 (1964). doi:10.1080/00288306.1964.10422108

38. O. Beyssac, M. Lazzeri, Application of Raman spectroscopy to the study of graphitic carbons in the Earth Sciences *EMU Notes Mineralogy*, **12**, 415–454 (2012).

39. A. Lahfid, O. Beyssac, E. Deville, F. Negro, C. Chopin, B. Goffé, Evolution of the Raman spectrum of carbonaceous material in low-grade metasediments of the Glarus Alps (Switzerland). *Terra Nova* **22**, 354–360 (2010). doi:10.1111/j.1365-3121.2010.00956.x

40. V. Galy, O. Beyssac, C. France-Lanord, T. Eglinton, Selective recycling of graphite during Himalayan erosion: A geological stabilisation of C in the crust. *Science* **322**, 943–945 (2008). Medline

41. J. Bouchez, O. Beyssac, V. Galy, J. Gaillardet, C. France-Lanord, L. Maurice, P. Moreira-Turcq, Oxidation of petrogenic organic carbon in the Amazon floodplain as a source of atmospheric CO_2. *Geology* **38**, 255–258 (2010). doi:10.1130/G30608.1

42. R. Sparkes, N. Hovius, A. Galy, R. V. Kumar, J. T. Liu, Automated analysis of carbon in powdered geological and environmental samples by Raman spectroscopy. *Appl. Spectrosc.* **67**, 779–788 (2013). Medline doi:10.1366/12-06826

43. E. Limpert, W. A. Stahel, M. Abbt, Log-normal distributions across the sciences: Keys and clues. *Bioscience* **51**, 341–352 (2001). doi:10.1641/0006-3568(2001)051[0341:LNDATS]2.0.CO;2

44. M. W. Mahaffy, A three-dimensional numerical model of ice sheets: Tests on the Barnes Ice Cap, Northwest Territories. *J. Geophys. Res.* **81**, 1059–1066 (1976). doi:10.1029/JC081i006p01059

45. K. Hutter, *Theoretical Glaciology: Material Science of Ice and the Mechanics of Glaciers and Ice Sheets* (D. Reidel Publishing/Tokyo, Terra Scientific Publishing, 1983).

46. K. B. Föllmi, K. Arn, R. Hosein, T. Adatte, P. Steinmann, Biogeochemical weathering in sedimentary chronosequences of the Rhône and Oberaar Glaciers (Swiss Alps): Rates and mechanisms of biotite weathering. *Geoderma* **151**, 270–281 (2009). doi:10.1016/j.geoderma.2009.04.012

47. W. W. Barker, S. A. Welch, J. F. Banfield, Biogeochemical weathering of silicate minerals. *Rev. Min.* **35**, 391–428 (1997).

48. J. Espitalié, G. Deroo, F. Marquis, La pyrolyse Rock-Eval et ses applications, première partie. *Rev. Inst. Fr. Pet.* **40**, 573–579 (1985).

49. E. Lafargue, F. Marquis, D. Pillot, Rock-Eval 6 applications in hydrocarbon exploration, production, and soil contamination studies. *Rev. Inst. Fr. Pet.* **53**, 421–437 (1998).

50. D. Sebag, J. R. Disnar, B. Guillet, C. Di Giovanni, E. P. Verrecchia, A. Durand, Monitoring organic matter dynamics in soil profiles by 'Rock-Eval pyrolysis': Bulk characterization and quantification of degradation. *Eur. J. Soil Sci.* **57**, 344–355 (2006). doi:10.1111/j.1365-2389.2005.00745.x

51. N. Hovius, C. P. Stark, P. A. Allen, Sediment flux from a mountain belt derived from landslide mapping. *Geology* **25**, 231–234 (1997). doi:10.1130/0091-7613(1997)025<0231:SFFAMB>2.3.CO;2

52. B. A. Clarke, D. W. Burbank, Bedrock fracturing, threshold hillslopes, and limits to the magnitude of bedrock landslides. *Earth Planet. Sci. Lett.* **297**, 577–586 (2010). doi:10.1016/j.epsl.2010.07.011

53. P. Nienow, M. Sharp, I. Willis, Seasonal changes in the morphology of the subglacial drainage system, Haut Glacier d'Arolla, Switzerland. *Earth Surf. Process. Landf.* **23**, 825–843 (1998). doi:10.1002/(SICI)1096-9837(199809)23:9<825::AID-ESP893>3.0.CO;2-2